16 Scanning Nonlinear Dielectric Microscope

Yasuo Cho

Research Institute of Electrical Communication, Tohoku University, Japan

Abstract

A sub-nanometer resolution scanning nonlinear dielectric microscope (SNDM) was developed for observing ferroelectric polarization. We also demonstrate that the resolution of SNDM is higher than that of a conventional piezo-response imaging. Secondly, we report new SNDM technique detecting higher nonlinear dielectric constants ϵ_{3333} and ϵ_{33333}. Higher order nonlinear dielectric imaging provides higher lateral and depth resolution. Thirdly, a new type of scanning nonlinear dielectric microscope probe, called the ϵ_{311}-type probe, and a system to measure the ferroelectric polarization component parallel to the surface were developed. Finally, the formation of artificial small inverted domain is reported to demonstrate that SNDM system is very useful as a nano-domain engineering tool. The nano-size domain dots were successfully formed in $LiTaO_3$ single crystal. This means that we can obtain a very high density ferroelectric data storage with the density above 1 Tbits/inch^2.

16.1 Introduction

Recently, ferroelectric materials, especially in thin film form, have attracted the attention of many researchers. Their large dielectric constants make them suitable as dielectric layers of microcapacitors in microelectronics. They are also investigated for application in nonvolatile memory using the switchable dielectric polarization of ferroelectric material. To characterize such ferroelectric materials, a high-resolution tool is required for observing the microscopic distribution of remanent (or spontaneous) polarization of ferroelectric materials.

With this background, we have proposed and developed a new purely electrical method for imaging the state of the polarizations in ferroelectric and piezoelectric material and their crystal anisotropy. It involves the measurement of point-to-point variations of the nonlinear dielectric constant of a specimen and is termed "scanning nonlinear dielectric microscopy (SNDM)" [1–7]. This is the first successful purely electrical method for observing the ferroelectric polarization distribution without the influence of the screening effect from free charges. To date, the resolution of this microscope has been improved down to the sub-nanometer order.

Here we describe the theory for detecting polarization and the technique for nonlinear dielectric response and report the results of the imaging of the ferroelectric domains in single crystals and thin films using SNDM. Especially in a measurement of PZT thin film, it was confirmed that the resolution was sub-nanometer order. We also describe the theoretical res-

Polar Oxides: Properties, Characterization, and Imaging
Edited by R. Waser, U. Böttger, and S. Tiedke

ISBN: 3-527-40532-1

olution of SNDM. Moreover, we demonstrate that the resolution of SNDM is higher than that of a conventional piezo-response imaging by using scanning force microscopy (SFM) technique [8, 9].

Next, we report new SNDM technique. In the above conventional SNDM technique, we measure the lowest order nonlinear dielectric constant ϵ_{333}, which is a 3rd rank tensor. To improve the performance and resolution of SNDM, we have modified the technique such that higher nonlinear dielectric constants ϵ_{3333} (4th rank tensor), ϵ_{33333} (5th rank tensor) are detected. It is expected that higher order nonlinear dielectric imaging will provide higher lateral and depth resolution. We confirmed this improvement over conventional SNDM imaging experimentally, and used the technique to observe the growth of a surficial paraelectric layer on periodically poled $LiNbO_3$ [10–12].

In addition to this technique, a new type of scanning nonlinear dielectric microscope probe, called the ϵ_{311}-type probe, and a system to measure the ferroelectric polarization component parallel to the surface have been developed. This is achieved by measuring the ferroelectric material's nonlinear dielectric constant ϵ_{311} instead of ϵ_{333}, which is measured in conventional SNDM. Experimental results show that the probe can satisfactorily detect the direction of the polarization parallel to the surface [13]. Finally, the formation of artificial small inverted domain is reported to demonstrate that SNDM system is very useful as a nano-domain engineering tool. The nano-size domain dots were successfully formed in $LiTaO_3$ single crystal. This means that we can obtain a very high density ferroelectric data storage with the density above Tbits/inch^2.

16.2 Nonlinear dielectric imaging with sub- nanometer resolution

First, we briefly describe the theory for detecting polarization. Precise descriptions of the principle of the microscope have been reported elsewhere (see [3, 4]). We also report the results of the imaging of the ferroelectric domains in single crystals and in thin films using the SNDM. Especially in the PZT thin film measurement, we succeeded to obtain a domain image with a sub-nanometer resolution.

16.2.1 Principle and theory for SNDM

Figure 16.1 shows the system setup of the SNDM using the LC lumped constant resonator probe [4]. In the figure, $C_s(t)$ denotes the capacitance of the specimen under the center conductor (the tip) of the probe. $C_s(t)$ is a function of time because of the nonlinear dielectric response under an applied alternating electric field E_{p3} (= $E_p \cos(\omega_p t)$, f_p = 5 − −100 kHz). The ratio of the alternating variation of capacitance $\Delta C_s(t)$ to the static value of capacitance C_{s0} without time dependence is given as [3]

$$\frac{\Delta C_s}{C_{s0}} = \frac{\epsilon_{333}}{\epsilon_{33}} E_p \cos(\omega_p t) + \frac{\epsilon_{3333}}{4\epsilon_{33}} E_p^2 \cos(2\omega_p t) \tag{16.1}$$

where ϵ_{33} is a linear dielectric constant and ϵ_{333} and ϵ_{3333} are nonlinear dielectric constants. The even rank tensor, including the linear dielectric constant ϵ_{33}, does not change with 180°

rotation of the polarization. On the other hand, the lowest order of the nonlinear dielectric constant ϵ_{333} is a third-rank tensor, similar to the piezoelectric constant, so that there is no ϵ_{333} in a material with a center of symmetry, and the sign of ϵ_{333} changes in accordance with the inversion of the spontaneous polarization.

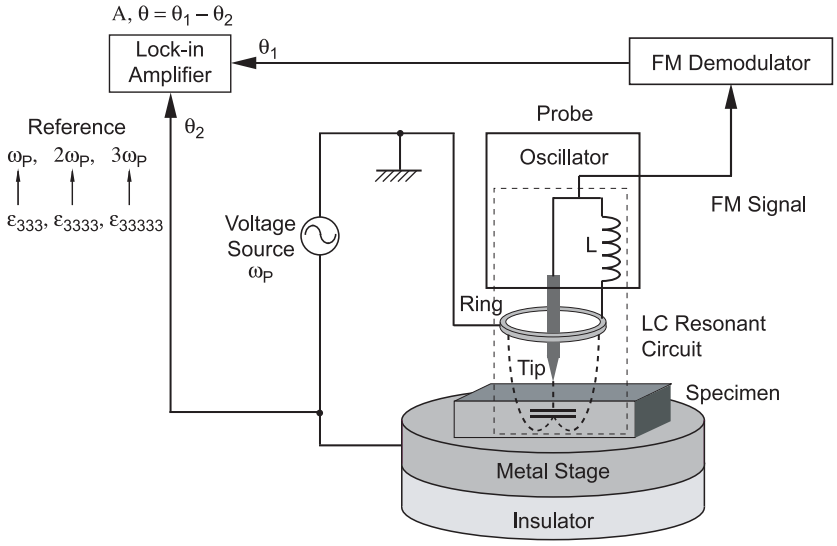

Figure 16.1: Schematic diagram of SNDM

This LC resonator is connected to the oscillator tuned to the resonance frequency of the resonator. The above mentioned electrical parts (i.e. tip, ring, inductance and oscillator) are assembled into a small probe for the SNDM. The oscillating frequency of the probe (or oscillator) (around 1.3 GHz) is modulated by the change of capacitance $\Delta C_s(t)$ due to the nonlinear dielectric response under the applied electric field. As a result, the probe (oscillator) produces a frequency modulated (FM) signal. By detecting this FM signal using the FM demodulator and lock-in amplifier, we obtain a voltage signal proportional to the capacitance variation. Each signal corresponding to ϵ_{333} and ϵ_{3333} was obtained by setting the reference signal of the lock-in amplifier at the frequency $2\omega_p$ of the applied electric field and at the doubled frequency $2\omega_p$, respectively. Thus we can detect the nonlinear dielectric constant just under the needle and can obtain the fine resolution determined by the diameter of the pointed end of the tip and the linear dielectric constant of specimens. The capacitance variation caused by the nonlinear dielectric response is quite small. ($\Delta C_s(t)/C_{s0}$ is in the range from 10^{-3} to 10^{-8}.) Therefore the sensitivity of SNDM probe must be very high. The measured value of the sensitivity of an above mentioned lumped constant probe is 10^{-22} F.

16.2.2 Nonlinear dielectric imaging

The tip of the lumped constant resonator probe was fabricated using electrolytic polishing of a tungsten wire or a metal coated conductive cantilever. The radius of curvature of the chip was 1 μm–25 nm. To check the performance of the new SNDM, first, we measured the macroscopic domains in a multidomain BTO single crystal. Figure 16.2 shows the two-dimensional image of the so called 90° a-c domain which is obtained by a coarse scanning over a large area. The sign of the nonlinear dielectric constant ϵ_{333} of the +c-domain is negative, whereas it is positive in the -c-domain.

Moreover the magnitude of $\epsilon_{111} = \epsilon_{222}$ is zero in the a-domain, because BTO belongs to tetragonal system at room temperature. Thus, we can easily distinguish the type of the domains.

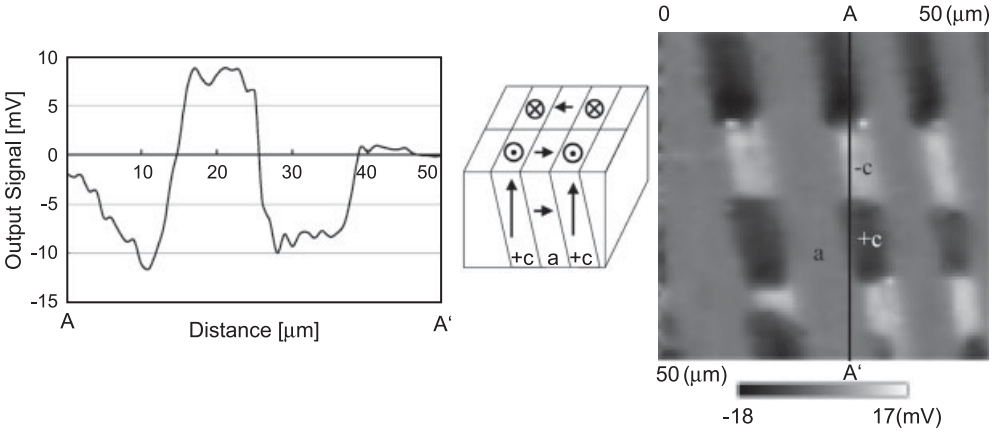

Figure 16.2: A two-dimensional image of the 90° a-c domain in a BTO single crystal and the cross-sectional (one- dimensional) image along the line A-A'.

To demonstrate that this microscopy is also useful for the domain measurement of thin ferroelectric films, we measured a PZT thin film. Figure 16.3 shows the SNDM (a) and AFM (b) images taken from a same location of PZT thin film deposited on a $SrTiO_3$ (STO) substrate using metal organic chemical vapor deposition.

From the figure, it is apparent that the film is polycrystalline (from Figure 16.3 (b)) and that each grain in the film is composed of several domains (from Figure 16.3 (a)). From X-ray diffraction analysis, this PZT film belongs to the tetragonal phase and the diffraction peaks, corresponding to both the c-axis and a-axis, were observed. Moreover, in Figure 16.3 (a), the observed signals were partially of zero amplitude, and partially positive. Thus, the images show that we succeeded in observing 90° a-c domain distributions in a single grain of the film.

These images of the film were taken from a relatively large area. Therefore, we also tried to observe very small domains in the same PZT film on STO substrate. The results are shown

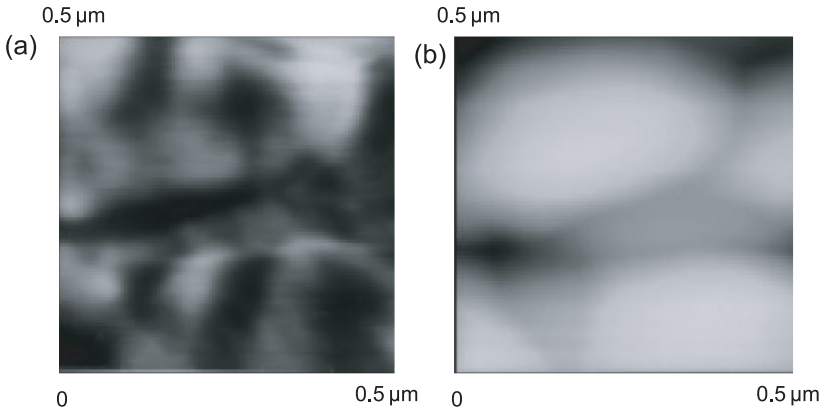

Figure 16.3: Images of a PZT film on a $SrTiO_3$ substrate. (a) Domain patterns by SNDM, (b) surface morphology by AFM.

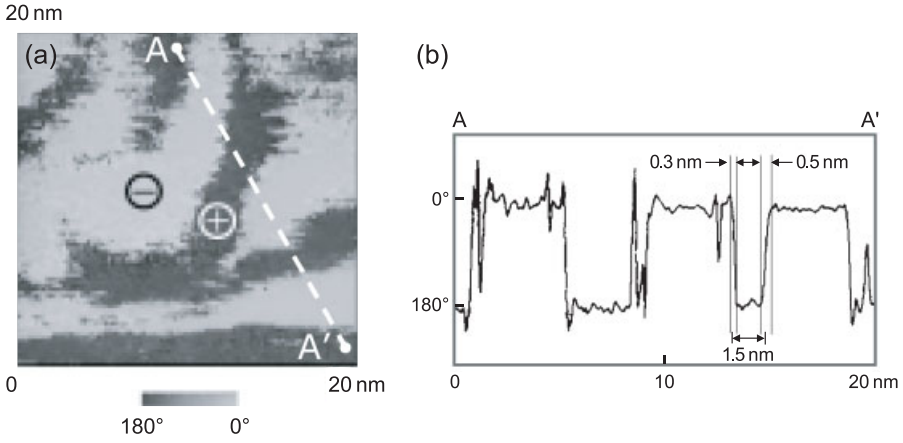

Figure 16.4: Nano-scale ferroelectric domain on PZT thin film, (a) domain image, (b) Cross sectional image of nano-scale 180° c-c domain, (one-dimensional) image of phase signal along the line A-A'.

in Figures 16.4 (a) and (b). The bright area and the dark area correspond to the negative polarization and the positive polarization, respectively. It shows that we can successfully observe a nano-scale 180° c-c domain structure. Figure 16.4 (b) shows a cross sectional image taken along line A-A' in Figure 16.4 (a). As shown in this figure, we measured the c-c domain with the width of 1.5 nm. Moreover we find that the resolution of the microscope is less than 0.5 nm.

However, as the above mentioned data shown in Figure 16.4 was phase images, some readers may think that the sub-nanometer resolution of SNDM is not convincingly proven in the references because phase profiles are invariably abrupt and can not be considered as the definition of the resolution and amplitude signals show more realistic resolution. Therefore, here, we show the amplitude images in Figure 16.5 to demonstrate the resolution of SNDM is really sub-nanometer order. These images were taken from an epitaxial PZT thin (4000 Å) / La-Sr-Co-O / $SrTiO_3$ [14]. The macroscopic surface topography and the domain pattern of this PZT thin film are shown in Figure 16.6. Square c-domains and their surrounding a-domain strip pattern are clearly observed.

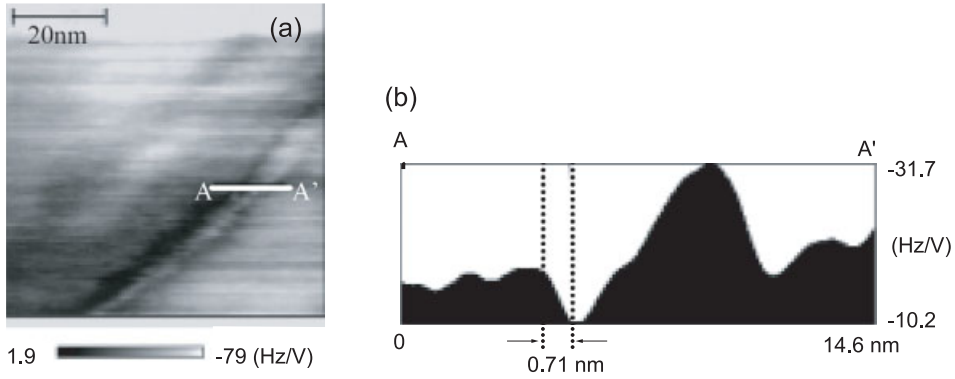

Figure 16.5: (a) Amplitude image of nanoscale ferroelectric domain on PZT thin film (b) Cross-sectional amplitude image taken along A-A'.

The strip shape domain pattern is seen in Figure 16.5. Figure 16.5 (b) is a cross sectional image taken along line A-A' in Figure 16.5 (a). From the distance between the clearly distinguishable structures in the image, it is apparent that SNDM has sub-nanometer resolution.

To clarify the reason why such high resolution can be easily obtained, even if a relatively thick needle is used for the probe, we show the calculated results of the one dimensional image of 180° c-c domain boundary lying at $y = 0$ (We chose y direction as the scanning direction) [15, 16]. Figure 16.7 shows the calculated results where Y_0 is the tip position normalized with respect to the tip radius a. The resolution of the SNDM image is heavily dependent on the dielectric constant of the specimen. For example, for the case of $\epsilon_{33}/\epsilon_0 = 1000$ and $a = 10\,\mathrm{nm}$, an atomic scale image will be able to be taken by SNDM.

16.2.3 Comparison between SNDM imaging and piezo-response imaging

Another frequently reported high-resolution tool for observing ferroelectric domains is piezoelectric response imaging using SFM [8, 9]. From the viewpoint of resolution for ferroelectric domains, SNDM will surpass the piezo-response imaging because SNDM measures the nonlinear response of a dielectric material which is proportional to the square of the electric field,

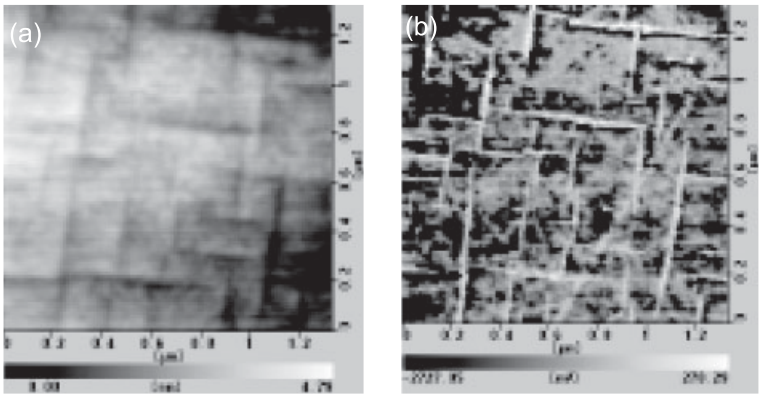

Figure 16.6: Macroscopic surface topography and domain pattern taken from an epitaxial PZT thin (4000 Å) / La-Sr-Co-O / $SrTiO_3$.

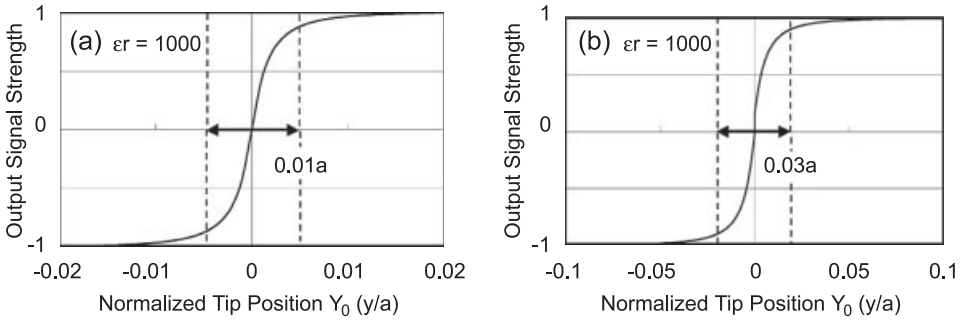

Figure 16.7: Theoretical images of the 180° c-c domain boundary.

whereas the piezoelectric response is linearly proportional to the electric field. The concentration of the distribution of the square of the electric field in the specimen underneath the tip is much higher than that of the linear electric field. Thus, SNDM can resolve smaller domains than that measured by piezo-imaging technique. To prove this fact experimentally, we also performed the simultaneous measurements of the same location of the above mentioned PZT film sample by using AFM (topography)- , SNDM- and piezo-imaging. The result is shown in Figure 16.8. These domain images were taken under identical conditions except that the applied voltage was $2V_{pp}$ in the SNDM imaging and $8V_{pp}$ in the piezo-imaging. In both SNDM image and piezo image, large negative signal was observed on the -c-domain and almost zero signal was detected on the a-domain, because there is a crystal symmetry along the depth direction on the a-domain. From the images, we can prove that SNDM can resolve greater detail than a conventional piezo-response imaging by using SFM technique.

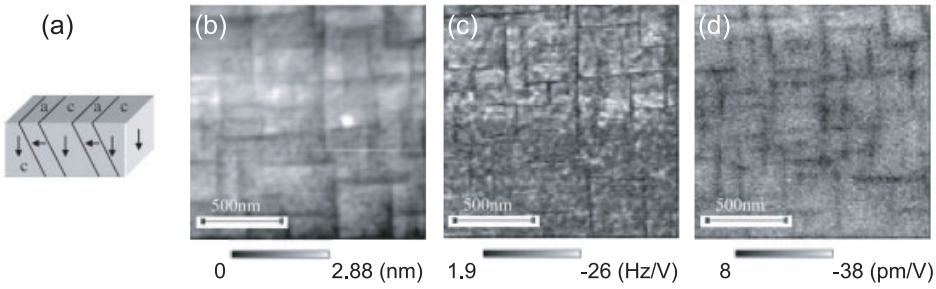

Figure 16.8: Simultaneously taken images of a PZT film. (a) Schematic domain structure (b) Topography by AFM, (c) domain patterns by SNDM, and (d) domain patterns by SFM (piezo-imaging).

16.2.4 Observation of domain walls in PZT thin film using SNDM

Several studies have examined the thickness of the domain wall in ferroelectric materials [17]. The 90° a-c domain wall thickness has been measured using a transmission electron microscope (TEM), [14] but distinguishing the positive and negative domains in 180° opposite polarization areas is difficult because these methods are used to observe the strain of arrangements of molecules. Direct clarification of the domain wall thickness is important with respect to both scientific and engineering aspects.

Therefore we observed the 90° a-c domain walls and the 180° c-c domain walls in the above mentioned same epitaxial PZT thin film grown on $SrTiO_3$ using SNDM.

The linear dielectric constant of a-domain is expected to be larger than that of c-domain based on the BTO single crystal analogy. To the authors' knowledge, no actual observation of linear dielectric constant of a- and c-domains in PZT has been reported. Because obtaining a PZT single crystal of sufficient size in order to compare the linear dielectric constant of a-domain and that of c-domain by the bulk method using a parallel plate capacitor is difficult. Therefore, at first, we measured the linear dielectric constant of a- and c-domains. The observation images are shown in Figure 16.9. In the linear dielectric constant measurements, we measure directly the frequency shifts immediately under the tip. If the high linear dielectric constant area is measured, the frequency shifts low. In Figure 16.9, we can see the frequencies in the a-domain areas are lower than those in the c-domain areas. So the linear dielectric constant of the a-domain is larger than that of the c-domain. The a-domain was first proven to have a higher linear dielectric constant than that of the c-domain just like $BaTiO_3$.

Next we observed the domain walls of 90° a-c and 180° c-c domains. Figure 16.10 (a) is a two-dimensional SNDM image of a-c domain and Figure 16.10 (b) is the cross-sectional image along the A-A' line in Figure 16.10 (a). In Figure 16.10 (b), the thickness of the boundary between a-domain and c1-domain was larger than that between a-domain and c2-domain. Moreover, according to the above-mentioned observation, a-domains have larger linear dielectric constants than c-domains. Therefore, the depth sensitivity at the a-domain becomes thinner than that at the c-domain. As a result, when the c-domain is measured, a signal of thicker area can be obtained than when the a-domain is measured. At the boundary between

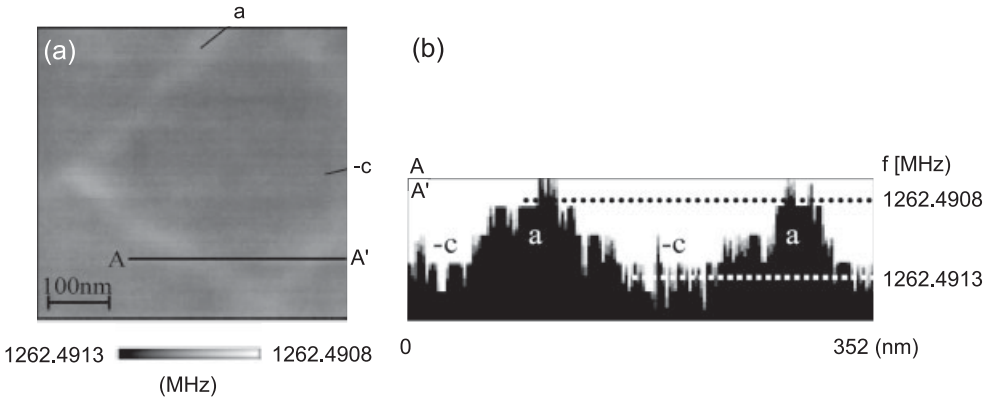

Figure 16.9: (a) Linear dielectric image of a-c domain in PZT, (b) cross-sectional image along the A-A' line.

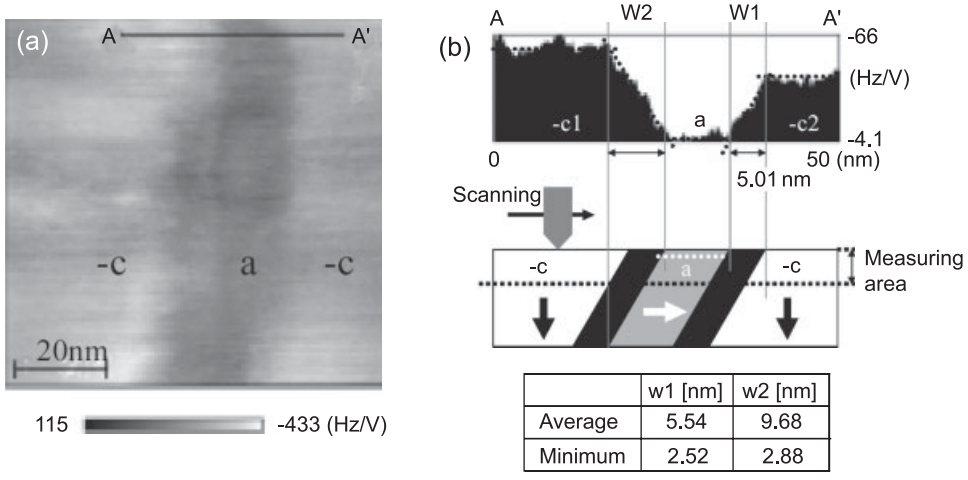

	w1 [nm]	w2 [nm]
Average	5.54	9.68
Minimum	2.52	2.88

Figure 16.10: (a) Image of a-c domain wall in PZT, (b) cross-sectional image of a-c domain along the A-A' line.

the c1-domain and the a-domain, the tip senses the a-domain under the c-domain before the tip reaches the real a-c domain boundary. As a result, the signal transition distance between c1-domain and a-domain becomes larger than the thickness of the actual a-c domain boundary. On the other hand, at the boundary between a-domain and c2-domain, the signal shows the change with no influence of c-domain under the a-domain, because the depth sensitivity at the a-domain is thinner then that at the c-domain. As a result, the distance between a-domain and c2-domain can be regarded as the actual a-c domain wall thickness. This wall thickness

was measured to be 5.01 nm, as shown in Figure 16.10 (b). The average thickness and minimum thickness of a-c domain wall were 5.54 nm and 2.52 nm, respectively. The minimum value seems to indicate the ideal domain wall thickness without the influences of the internal electric field or the residual stress stored in the boundary.

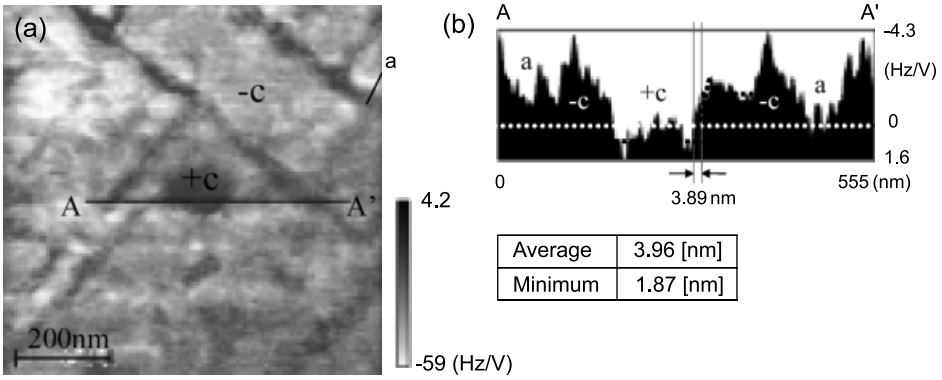

Figure 16.11: (a) Image of c-c domain wall in PZT, (b) cross-sectional image of c-c domain along the A-A' line.

In a similar way, we observed the domain wall between the 180° c-c domains. Before observation, we applied +10 V voltage to the -c domain area to make the +c domain area. Figure 16.11 (a) shows the two-dimensional SNDM image. The dark area in the center of the image is the +c domain area. Figure 16.11 (b) is a cross-sectional image along line A-A' shown in Figure 16.11 (a). The thickness of the c-c domain wall is 3.89 nm in this image. The average thickness and minimum thickness of the c-c domain wall were 3.95 nm and 1.87 nm, respectively. The c-c domain wall had a size of a few unit cells.

In the case of the a-c domain wall, the boundary of a-domain and c-domain is constructed to include lattice strain in order to match the length of the a-axis and the c-axis. On the other hand, in the case of the c-c domain wall, the lattice lengths do not need to match. Therefore, the c-c domain wall does not contain strain, which depends on lattice mismatching. As a result, the c-c domain wall appears to be smaller than the a-c domain wall. Based on the above result, we determined experimentally that the 180° c-c domain wall is thinner than the 90° a-c domain wall.

16.3 Higher order nonlinear dielectric microscopy

A higher order nonlinear dielectric microscopy technique with higher lateral and depth resolution than conventional nonlinear dielectric imaging is investigated. The technique is demonstrated to be very useful for observing surface layers of the order of unit cell thickness on ferroelectric materials.

16.3.1 Theory for higher order nonlinear dielectric microscopy

Equation (16.2) is a polynomial expansion of the electric displacement D_3 as a function of electric field E_3.

$$D_3 = P_{s3} + \epsilon_{33}E_3 + \frac{1}{2}\epsilon_{333}E_3^2 + \frac{1}{6}\epsilon_{3333}E_3^3 + \frac{1}{24}\epsilon_{33333}E_3^4 + ... \tag{16.2}$$

Here, ϵ_{33}, ϵ_{333}, ϵ_{3333}, and ϵ_{33333} correspond to linear and nonlinear dielectric constants and are tensors of rank 2nd, 3rd, 4th and 5th, respectively. Even-ranked tensors including linear dielectric constant ϵ_{33} do not change with polarization inversion, whereas the sign of the odd-ranked tensors reverses. Therefore, information regarding polarization can be elucidated by measuring odd-ranked nonlinear dielectric constants such as ϵ_{333} and ϵ_{33333}.

Considering the effect up to E^4, the ratio of the alternating variation of capacitance ΔC_s underneath the tip to the static capacitance C_{s0} is given by

$$\frac{\Delta C_s}{C_{s0}} \approx \frac{e_{333}}{e_{33}}E_p\cos(\omega_p t) + \frac{1}{4}\frac{e_{3333}}{e_{33}}E_p^2\cos(2\omega_p t) + \frac{1}{24}\frac{e_{33333}}{e_{33}}E_p^3\cos(3\omega_p t) + ... \tag{16.3}$$

This equation shows that the alternating capacitance of different frequencies corresponds to each order of the nonlinear dielectric constant. Signals corresponding to ϵ_{333}, ϵ_{3333} and ϵ_{33333} were obtained by setting the reference signal of the lock-in amplifier in Figure 16.1 to frequency ω_p, 2 ω_p and 3 ω_p of the applied electric field, respectively.

Next, we consider the resolution of SNDM. From (16.2), the resolution of SNDM is found to be a function of electric field E. We note that the electric field under the tip is more highly concentrated with the increase of ϵ_{33} [18], and the distributions of E^2, E^3 and E^4 fields underneath the tip become much more concentrated in accordance with their power than that of the E field, as shown in Figure 16.12. From this figure, we find that higher order nonlinear dielectric imaging has higher resolution than lower order nonlinear dielectric imaging.

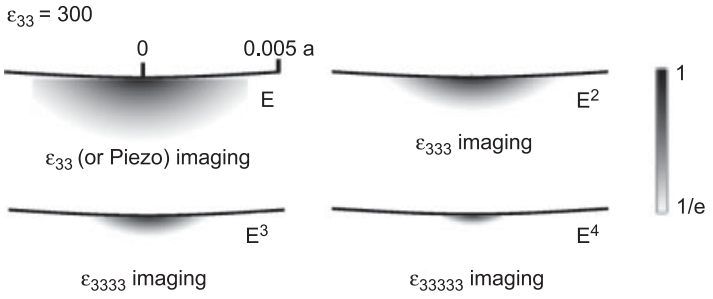

Figure 16.12: Distribution of E, E^2, E^3 and E^4 field under the needle tip. a denotes the tip radius.

16.3.2 Experimental details of higher order nonlinear dielectric microscopy

We experimentally confirmed that ϵ_{33333} imaging has higher lateral resolution than ϵ_{333} imaging using an electroconductive cantilever as a tip with a radius of 25 nm. Figures 16.13 (a) and (b) show ϵ_{333} and ϵ_{33333} images of the two-dimensional distribution of lead zirconate titanate PZT thin film. The two images can be correlated, and it is clear that the ϵ_{33333} image resolves greater detail than ϵ_{333} image due to the higher lateral and depth resolution.

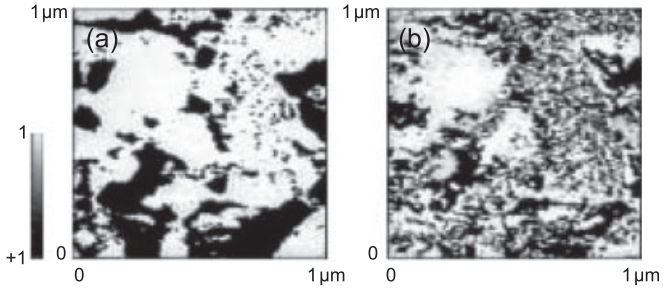

Figure 16.13: (a) ϵ_{333} and (b) ϵ_{33333} images of PZT thin film.

Next, we investigated the surface layer of periodically poled $LiNbO_3$ (PPLN) by ϵ_{333}, ϵ_{3333} and ϵ_{33333} imaging. Figure 16.14 (a) shows ϵ_{333}, ϵ_{3333} and ϵ_{33333} signals of virgin unpolished PPLN. In this figure, only ϵ_{333} imaging detects the c-c domain boundary, while ϵ_{33333} imaging does not. The ϵ_{3333} signal shows weak peaks at domain boundaries. This is because ϵ_{3333} and ϵ_{33333} imaging is affected by the surface paraelectric layer. To prove the existence of a surface paraelectric layer, we polished and measured the PPLN. Figure 16.14 (b) shows the images of it. In this figure, it is clear that ϵ_{33333} imaging can detect the c-c domain boundary after removal of the paraelectric layer. Moreover, ϵ_{3333} imaging can also detect periodic signals, in contrast to our expectation. The nonlinear dielectric signals of a positive area of PPLN are stronger than those of a negative area immediately after polishing, possibly because the negative area is more easily damaged than positive area and has already been covered by a very thin surface paraelectric layer with weak nonlinearity even immediately after polishing. One hour after polishing, we conducted the ϵ_{333}, ϵ_{3333} and ϵ_{33333} imaging again, and the results are shown in Figure 16.14 (c). In this figure, the ϵ_{33333} signal disappears and the ϵ_{3333} signal becomes flat again, whereas ϵ_{333} imaging clearly detects the c-c domain boundary (Figure 16.14 (a)). This implies that the entire surface area of PPLN is covered by the surface paraelectric layer again. From theoretical calculations, on the $LiNbO_3$ substrate, ϵ_{33333} and ϵ_{3333} imagings have sensitivities down to 0.75 nm depth and 1.25 nm, respectively, whereas ϵ_{333} imaging has sensitivity down to 2.75 nm depth when a tip of 25 nm radius is used. Thus, we conclude that the thickness of this surface paraelectric layer ranges between 0.75 nm and 2.75 nm.

From these results, we succeed in observing the growth of the surface layer and we confirm that the negative area of $LiNbO_3$ can be more easily damaged than the positive area.

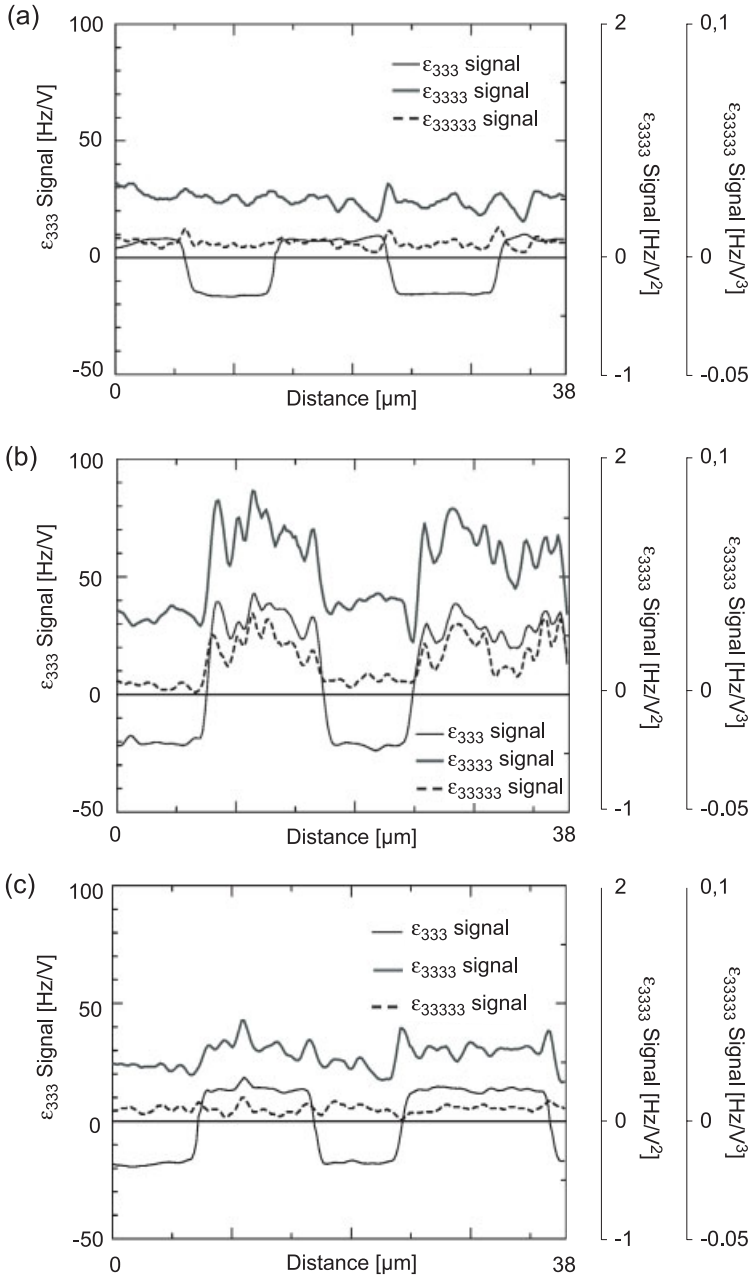

Figure 16.14: (a) ϵ_{333}, ϵ_{3333} and ϵ_{33333} images of virgin PPLN, (b) immediately after polishing, and (c) 1 h after polishing.

16.4 Three-dimensional measurement technique

A new type of scanning nonlinear dielectric microscope (SNDM) probe, named ϵ_{311} type probe, and a system to measure the ferroelectric polarization component parallel to the surface using SNDM has been developed [19]. This is achieved by measuring a nonlinear dielectric constant of ferroelectric material ϵ_{311} instead of ϵ_{333}, which is measured in conventional SNDM. Experimental results show that the probe can detect the polarization direction parallel to the surface with high spatial resolution. Moreover, we propose an advanced measurement technique using rotating electric field. This technique can be applied to measure three-dimensional polarization vectors.

16.4.1 Principle and measurement system

Figure 16.15 shows parallel plate models of nonlinear dielectric constant measurements. Since precise descriptions of the ϵ_{333} measurement have been mentioned above, we explain only the ϵ_{311} measurement. We consider the situation in which a relatively large electric field $\bar{E}_3$ with the amplitude E_p and angular frequency ω_p is applied to the capacitance C_s, producing a change of the capacitance resulting from the nonlinear dielectric response. We detect the capacitance variation ΔC_s, which is perpendicular to the polarization direction (z-axis) by a high frequency electric field with small amplitude along x-axis ($\tilde{E}_1$) as shown in Figure 16.15 (b). (In the ϵ_{333} measurement, we detect ΔC_s along the direction of spontaneous polarization P_{s3}.) That is, in the ϵ_{311} measurement, $\bar{E}$ is perpendicular to $\tilde{E}$. We call this kind of measurements, which use the crossed electric field, "ϵ_{311} type" measurement. In this case, final formula is given by

$$\frac{\Delta C_s(t)}{C_{s0}} \approx \frac{e_{311}}{e_{11}} E_p \cos(\omega_p t) + \frac{1}{4} \frac{e_{3311}}{e_{11}} E_p^2 \cos(2\omega_p t) \tag{16.4}$$

where ϵ_{11} is the linear dielectric constant, and ϵ_{311} and ϵ_{3311} are nonlinear dielectric constants. From this equation, by detecting the component of capacitance variation with the angular frequency of the applied electric field ω_p, we can detect the nonlinear dielectric constant ϵ_{311}. According to this principle, we develop a ϵ_{311} type probe for measuring the polarization direction parallel to the surface. Figure 16.16 shows a schematic diagram of the measurement system. We put 4 electrodes around the probe tip to supply the electric field $\bar{E}$, which causes the nonlinear effect. The electrode A and B supply $\bar{E}_3$, which is along the z-axis, and electrode C and D supply $\bar{E}_2$, which is along the y-axis. We apply voltages to the electrodes, as satisfying the condition that, $\bar{E}_3$ and $\bar{E}_2$ just under the tip become parallel to the surface without concentrating at the tip as shown in Figure 16.16 (b). (In Figure 16.16 (b) the component related to y-direction are omitted for simplification.) On the other hand, the electric field $\tilde{E}$ for measuring the capacitance variation concentrates at the probe tip as the conventional measurement. It is sufficient to consider only x- component of $\tilde{E}$, because we confirmed that most of $\tilde{E}$ underneath the tip is perpendicular to the surface.

Moreover, we can obtain any electric field vector $\bar{E}$ with arbitrary rotation angle by combining the amplitude of $\bar{E}_2$ and $\bar{E}_3$. Therefore, we need not to rotate the specimen for detecting a lateral polarization with an arbitrary direction.

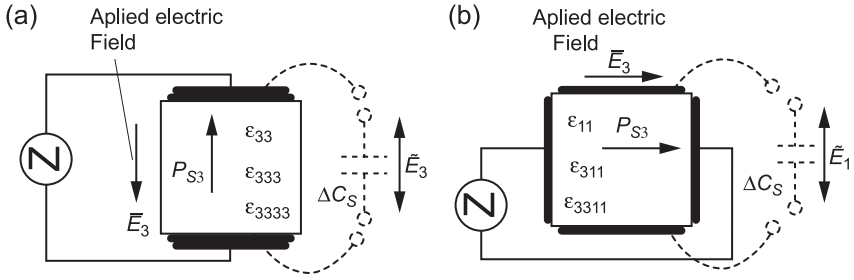

Figure 16.15: Capacitance variation with alternating electric field. (a) ϵ_{333} measurement, and (b) ϵ_{333} measurement.

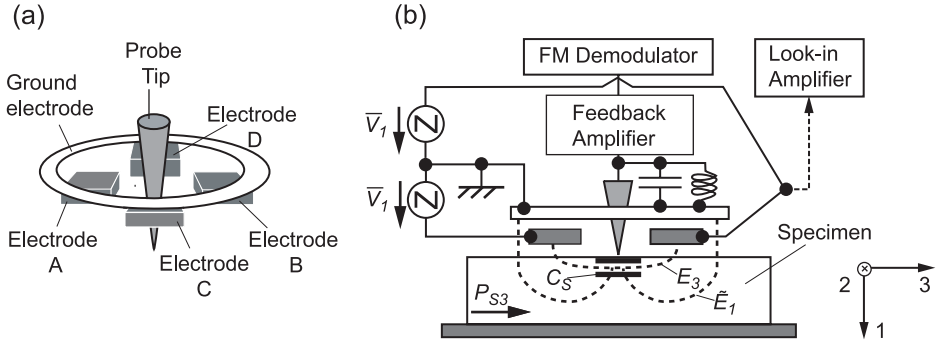

Figure 16.16: Schematic configuration of (a) new ϵ_{311} probe and (b) measurement system.

16.4.2 Experimental results

Figure 16.17 shows measurement result of PZT thin film as changing the direction of applied electric field $\bar{E}$. In Figure 16.17 (a), when $\bar{E}$ is parallel to the polarization direction, the pattern corresponding to the polarization is observed, while no pattern is observed in Figure 16.17 (b) because, in this case, $\bar{E}$ is perpendicular to the polarization direction. Figures 16.17 (c) and (d) are the cases where $\bar{E}$ is applied along the intermediate direction. The pattern can be observed from both Figures 16.17 (c) and (d), because the vector $\bar{E}$ can be divided by the component along the polarization direction. However the opposite contrast was obtained because the signs of the component along the polarization are opposite.

Moreover, the new probe can measure both ϵ_{311} and ϵ_{333} independently. Figure 16.17 (e) shows an ϵ_{333} image, which corresponds to the perpendicular component of the polarization. From the same position in Figure 16.17 (a), signals are observed. It means that this polarization has both parallel and perpendicular component, that is, the polarization tilts from the surface. Figure 16.17 (f) is a topography, which is also measured simultaneously. From these

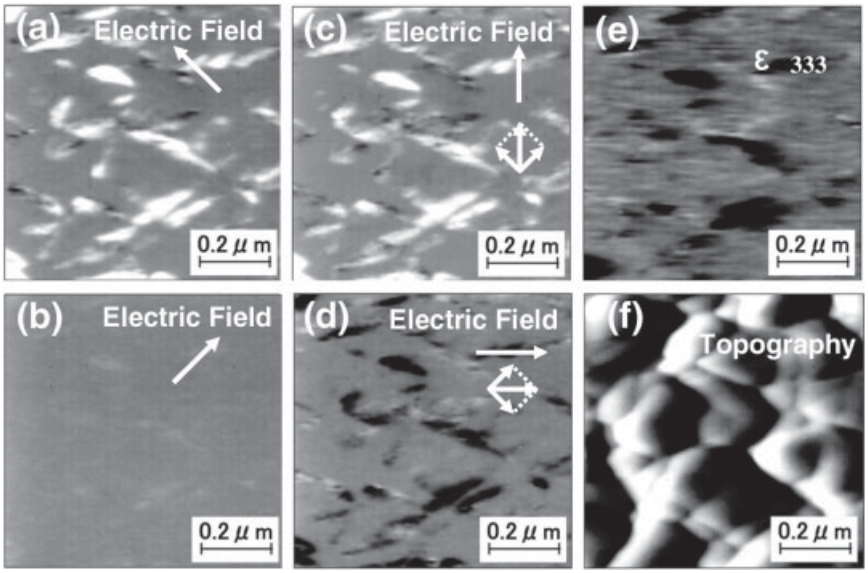

Figure 16.17: Images of PZT thin film, (a)–(d) ϵ_{311} images, (e) ϵ_{333} image, and (f) topography.

results, we confirmed that the new probe and system can be applied to the 3-dimensional polarization measurements.

Based on this technique, we have developed a more advanced method to measure the distribution of polarization directions parallel to the surface. We use a rotating electric field by applying a 90° phase shifted electric voltage between the electrodes A, B, and C, D; that is, we apply the electric fields $\bar{E}_3 = E\cos\omega_p t$ and $\bar{E}_2 = E\cos\omega_p t$ just under the probe tip of Figure 16.16. Under this condition, the electric field rotates with an angular frequency of ω_p and the amplitude of the capacitance variation is changed periodically. When the electric field is parallel to the polarization direction, the capacitance variation is at a maximum, and when the electric field is perpendicular to the polarization direction, the capacitance variation is at a minimum. Consequently, if we detect the capacitance variation by a lock-in amplifier using a reference signal of angular frequency ω_p, we can obtain the angle of the polarization direction directly from the phase output of the lock-in amplifier. Figure 16.18 shows the measurement results on a PZT thin film using a rotating electric field. Histogram of the measured data clearly shows three peaks, which correspond to 0°, 90° and 180°. In Figure 16.18, we can see these three regions. One region is white and black. Within the white and black regions, the white parts and the black parts show the polarization directions +180° and -180°, respectively. Therefore these regions can be considered to be the same domain. Another region is dark gray. The polarization direction in this region is 0°. The third region is bright gray, where the polarization direction is 90°. We suppose that the reasons why a -90° region does not exist are related to a film growth condition. The polarization direction for each region is shown by arrows. The domain structure of this figure is not the typical 90° a-c domain and 180° c-c

domain which is usually seen in PZT ceramics. This is because the sample is a thin film. Since the grain size of this film is about 300 nm, Figure 16.18 shows the polarization distribution in a grain. We suppose that the domain structure in a grain depends on a film growth condition. As shown in this figure, we could successfully observe the domain structure, showing the different directions of the polarization parallel to the surface with high spatial resolution.

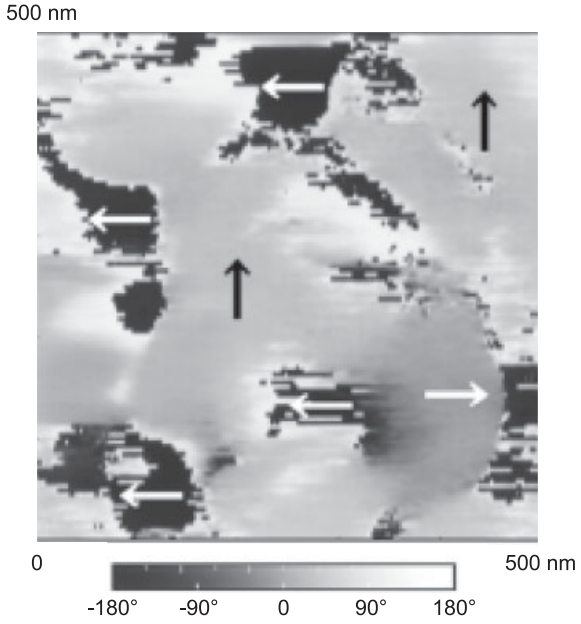

Figure 16.18: Image of a PZT thin film measured by SNDM using rotating electric field.

16.5 Ultra High-Density Ferroelectric Data Storage Using Scanning Nonlinear Dielectric Microscopy

Ferroelectrics have created considerable interest as promising storage media. Here, an investigation for ultra high-density ferroelectric data storage based on scanning nonlinear dielectric microscopy (SNDM) was carried out. For the purpose of obtaining the fundamental knowledge of high-density ferroelectric data storage, several experiments of nano-domain formation in lithium tantalate ($LiTaO_3$) single crystal were conducted. As a result, very small inverted domain with radius of 6 nm was successfully formed in stoichiometric $LiTaO_3$ (SLT), and besides, domain dot array with areal density of 1.5 Tbit/inch^2 was written in congruent $LiTaO_3$ (CLT).

16.5.1 SNDM domain engineering system

Figure 16.19 shows the schematic diagram of SNDM domain engineering system. The probe is composed of a metal-coated conductive cantilever (typical tip radius is 25 nm), an oscillator and a grounded metal ring. Polarity distinction is performed by SNDM technique. On the other hand, writing is performed by applying relatively large voltage pulse to the specimen and locally switching the polarization direction.

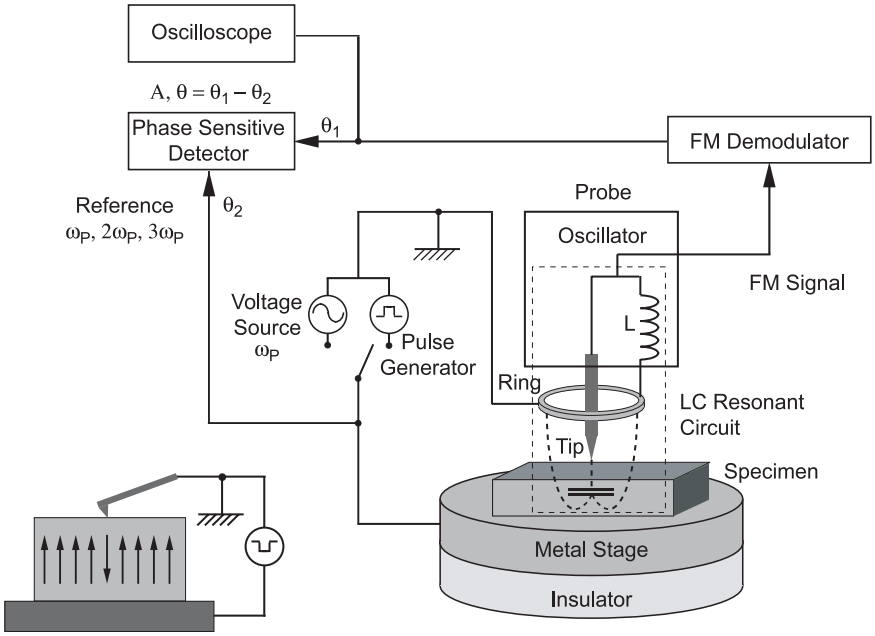

Figure 16.19: Schematic diagram of SNDM domain engineering system.

16.5.2 Nano-domain formation in $LiTaO_3$ single crystal

In this study, we selected $LiTaO_3$ single crystal as a recording medium because this material has suitable characteristics as follows:

(1) There exist only 180° c-c domains.

(2) It does not possess transition point near room temperature.

(3) High-quality and large single crystal can be fabricated at low cost.

At the present time, two types of $LiTaO_3$ single crystals are widely known; one is stoichiometric $LiTaO_3$ (SLT) [20] and the other is congruent $LiTaO_3$ (CLT). It is reported that domain inversion characteristics of these crystals are distinctly different each other [21–23]. SLT has

few pinning sites of domain switching derived from Li point defects. Therefore, SLT has the characteristics that the coercive field is low and the switching time is short. This means that SLT is favorable for low-power and high-speed writing.

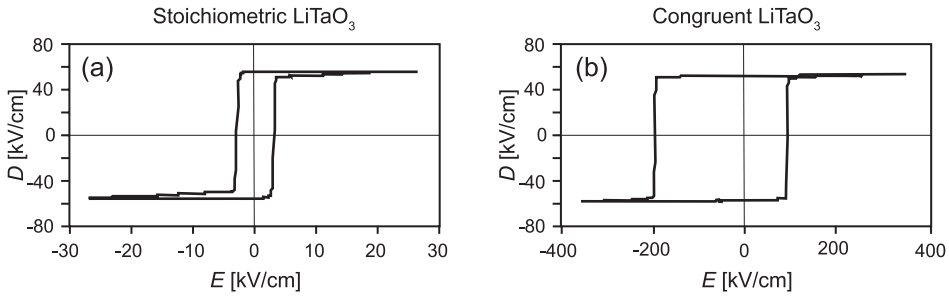

Figure 16.20: D-E hysteresis loop of $LiTaO_3$ measured by applying 10 mHz triangular wave voltage.

Figure 16.20 shows D-E hysteresis of SLT and CLT measured by applying 10 mHz triangular wave voltage, and lower coercive field of SLT compared with that of CLT can be confirmed. On the other hand, CLT has many pinning sites because it is Ta-rich crystal, and it is known that natural domain size of CLT is much smaller than that of SLT. Therefore, we expect that CLT is suitable for higher density storage with smaller domain dots. In the case of forming inverted domain by means of applying voltage to a specimen using a sharp-pointed tip, electric field is highly concentrated just under the tip. So, if the specimen is very thick as compared to the tip radius, large voltage is required for domain switching. Therefore, making thin specimens is very important. In this study, we prepared specimens with thickness of about 100 nm.

Figure 16.21 shows SNDM images of typical nano-sized inverted domains formed in a 100 nm thick SLT medium by means of applying voltage pulses with amplitude of 15 V and duration time of (a) 500 ns (b) 100 ns (c) 60 ns. From these figures, we found that the area of the domain decreases with decreasing voltage application time.

The dependence of domain size on voltage application time is derived from sidewise motion of domain wall. More detailed experimental result with regard to the relationship between the radius of the inverted domain and voltage application time is shown in Figure 16.22.

Figure 16.23 shows the smallest inverted domain at the present time. The radius of this domain is 6 nm, which corresponds to storage density of 4 Tbit/inch^2 if more than one dot can be formed in close-packed array. The result of studying the retention of small inverted domains is depicted in Figure 16.24. These images are observed (a) 50 minutes after pulse application (b) 8 hours after pulse application (c) 24 hours after pulse application. From this result, we found that small inverted domains remained stably for a long time.

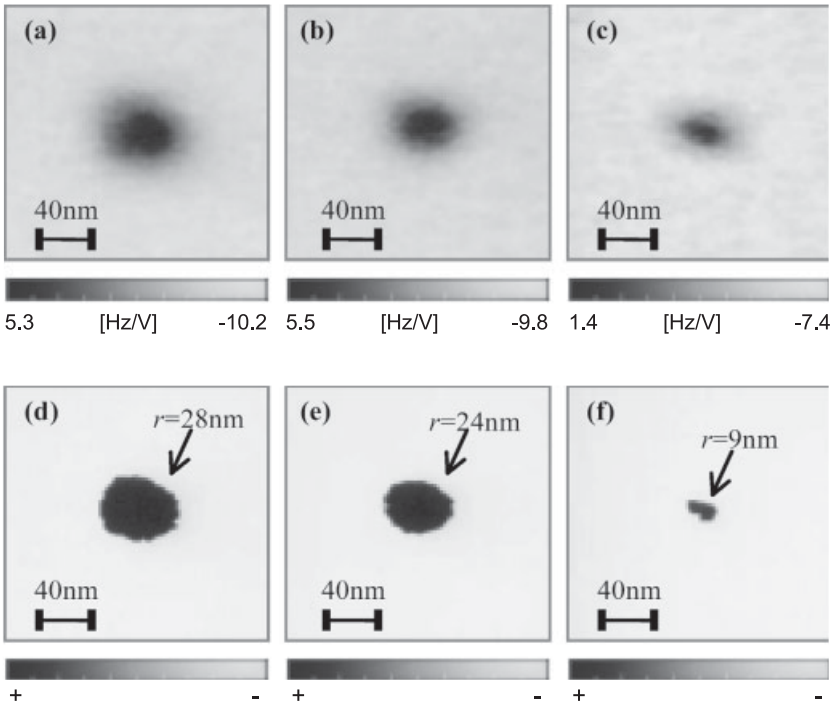

Figure 16.21: Images of typical inverted domains formed in SLT by means of applying a voltage pulse with amplitude of 15 V and duration time of (a), (d) 500 ns, (b), (e) 100 ns, (c), (f) 60 ns. (a)–(c) $\cos\Theta$ images, (d)-(f) polarity images.

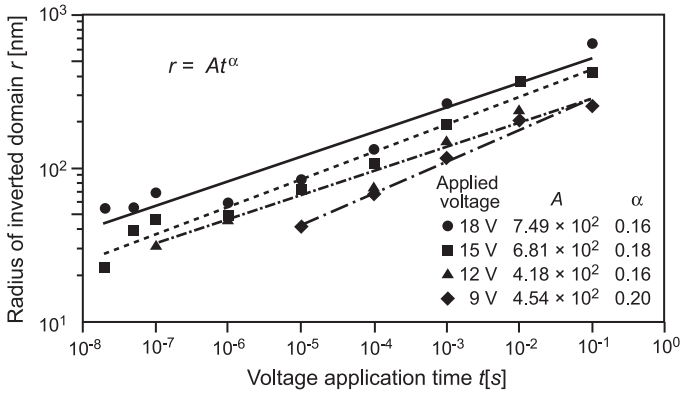

Figure 16.22: Relationship between the radius of the inverted domain and voltage application time in SLT. Sample thickness is 250 nm.

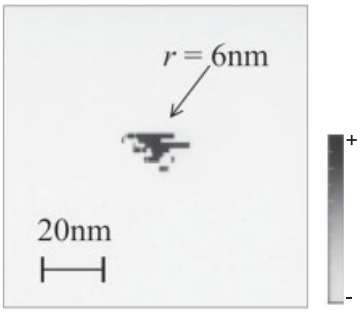

Figure 16.23: The smallest inverted domain at the present time, which was formed in 100 nm thick SLT by applying 15 V, 60 ns pulse.

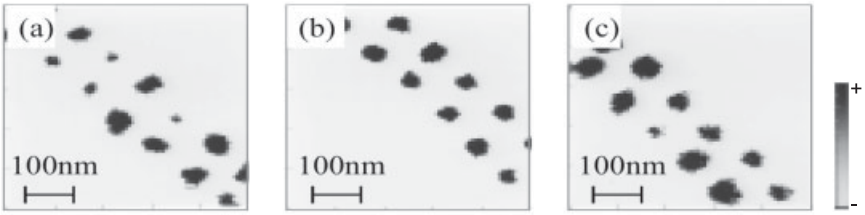

Figure 16.24: Images of inverted domain dot array in 150 nm thick SLT. These images are observed (a) 50 minutes after pulse application (b) 8 hours after pulse application (c) 24 hours after pulse application.

Figure 16.25 shows the relationship between the radius of the inverted domain and voltage application time in SLT and CLT. Voltage application time required for forming a certain size of domain in SLT and CLT are different by five to six orders of magnitude. This difference in switching time is derived from the difference in the number of domain pinning sites. Short switching time in SLT is favorable for low-power and high-speed writing. Subsequently, we conducted some experiments of forming any domain shape by means of applying voltage pulses in multipoint while controlling the probe position.

Figure 16.26 shows the domain characters "TOHOKU UNIV." written in SLT and CLT. The inverted domain in Figure 16.26 (a) was formed in 150 nm thick SLT by applying 15 V, 100 ns voltage pulses, and the inverted domain in Figure 16.26 (b) was formed in 70 nm thick CLT by applying 14 V, 10 μs voltage pulses for the left figure and 14 V, 5 μs voltage pulses for the right figure. From these figures, we found that small inverted domain pattern was successfully formed in CLT despite of applying relatively long pulses on a thinner sample. This result is vividly reflects that pinning sites derived from lithium nonstoichiometry prevent the sidewise motion of domain walls. Thereby, we verified the feasible storage density using CLT.

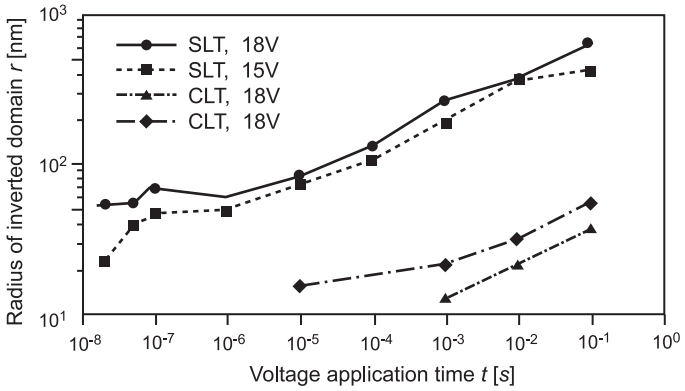

Figure 16.25: Relationship between the radius of the inverted domain and voltage application time in SLT and CLT. Sample thickness is 250 nm.

Figure 16.27 shows images of the inverted domain pattern in CLT with density of (a) 0.62 Tbit/inch^2 (b) 1.10 Tbit/inch^2 (c) 1.50 Tbit/inch^2. These domain patterns were formed by applying voltage pulses with amplitude of (a) 11 V (b),(c) 12 V and duration time of (a) 10 μs (b) 500 ns (c) 80 ns. Close-packed dot array composed of positive and negative domain can be seen in these figures.

Although the dots in the 1.50 Tbit/inch^2 array may not be resolvable with sufficient accuracy for practical data storage, this system is fully expected to become practically applicable as a storage system after further refinement. We have thus demonstrated, using a ferroelectric medium and nano-domain engineering, that rewritable bit storage at a data density of more than 1 Tbit/inch^2 is achievable. To the best of our knowledge, this is the highest density reported for rewritable data storage, and is expected to stimulated renewed interest in this approach to next-generation ultrahigh-density rewritable electric data storage systems.

16.6 Conclusions

In this paper, first, a sub-nanometer resolution scanning nonlinear dielectric microscope (SNDM) for the observation of ferroelectric polarization was described. We also demonstrated that the resolution of SNDM is higher than that of a conventional piezo-response imaging. Using SNDM, we measured the wall thickness of PZT thin film. We also described the theoretical resolution of SNDM. This theoretical result predicted that an atomic scale image can be taken by SNDM.

Next, we reported new SNDM technique detecting higher nonlinear dielectric constants ϵ_{3333} and ϵ_{33333}. It is expected that higher order nonlinear dielectric imaging will provide higher lateral and depth resolution. Using this higher order nonlinear dielectric microscopy technique, we successfully investigated the surface layer of ferroelectrics. Moreover, a new

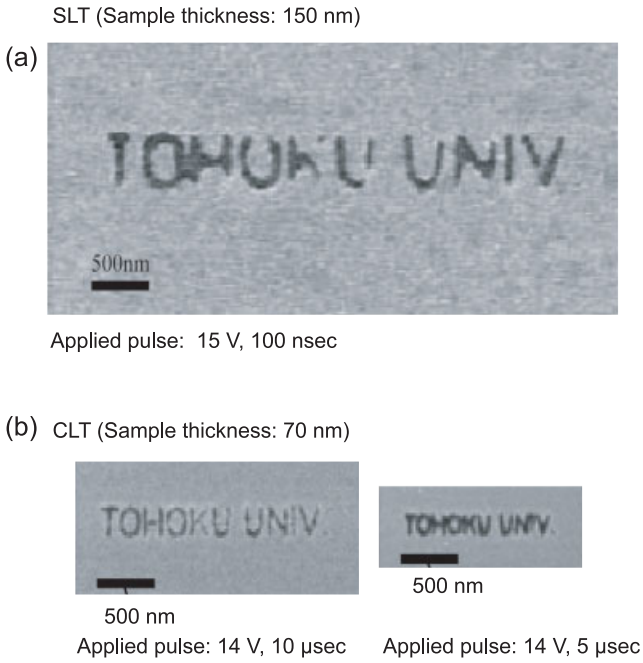

Figure 16.26: Nano-domain characters "TOHOKU UNIV." written in (a) SLT and (b) CLT.

type of scanning nonlinear dielectric microscope probe, called the ϵ_{311}-type probe, and a system to measure the ferroelectric polarization component parallel to the surface was developed.

Finally, the formation of artificial small inverted domain was reported to demonstrate that SNDM system is very useful as a nano-domain engineering tool. The nano-size domain dots were successfully formed in $LiTaO_3$ single crystal. This means that we can obtain a very high density ferroelectric data storage with the density above 1 Tbits/inch^2.

Therefore, we have concluded that the SNDM is very useful for observing ferroelectric nano domain and local crystal anisotropy of dielectric material with sub-nano meter resolution and also has a quite high potential as a nano-domain engineering tool.

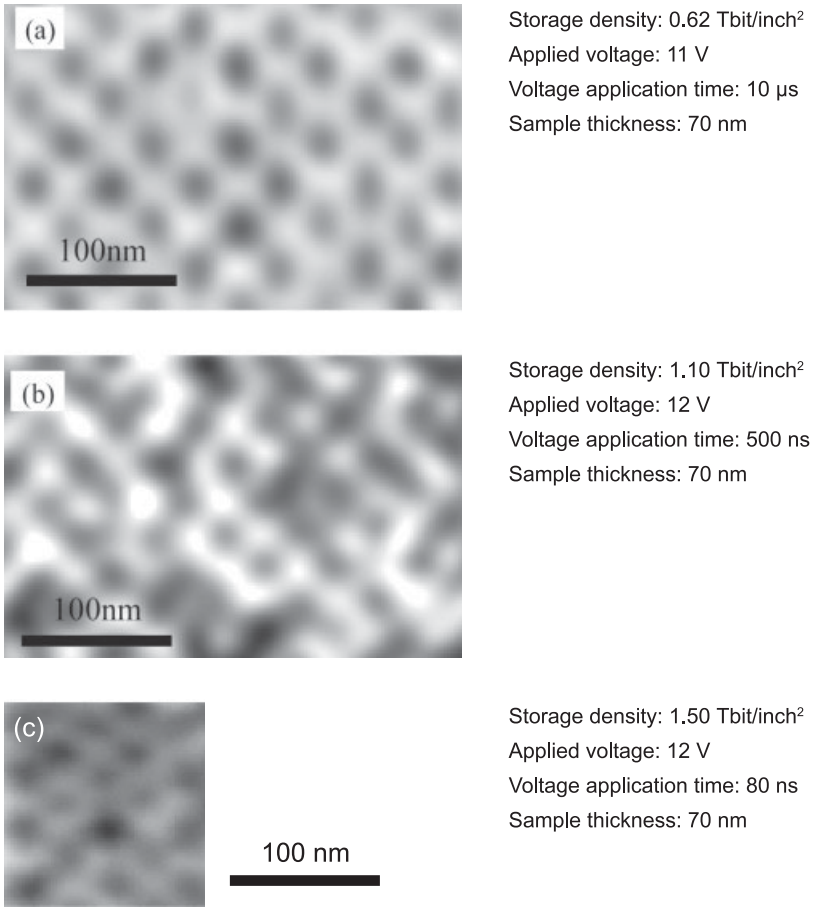

Figure 16.27: Images of the inverted domain pattern formed in CLT with density of (a) 0.62 Tbit/inch^2 (b) 1.10 Tbit/inch^2 (c) 1.50 Tbit/inch^2.

Acknowledgement

We would like to sincerely thank Prof. H. Funakubo of Tokyo Institute of Technology and Prof. R. Ramesh of University of Maryland for supplying the PZT thin film samples.

Bibliography

[1] Y. Cho, A. Kirihara, and T. Saeki, *Denshi Joho Tsushin Gakkai Ronbunshi* **J78-C-1**, 593 (1995) [in Japanese].

[2] Y. Cho, A. Kirihara and T. Saeki, *Electronics and Communication in Japan*, Part 2, **79**, Scripta Technica, Inc., 68 (1996).

[3] Y. Cho, A. Kirihara and T. Saeki, *Rev. Sci. Instrum.* **67**, 2297 (1996).

[4] Y. Cho, S. Atsumi and K. Nakamura, *Jpn. J. Appl. Phys.* **36**, 3152 (1997).

[5] Y. Cho, S. Kazuta and K. Matsuura, *Appl. Phys. Lett.* **72**, 2833 (1999).

[6] H. Odagawa and Y. Cho, *Surface Science* **463**, L621 (2000).

[7] H. Odagawa and Y. Cho, *Jpn. J. Appl. Phys.* **39**, 5719 (2000).

[8] A. Gruverman, O. Auciello, R. Ramesh, and H. Tokumoto, *Nanotechnology* **8**, A38 (1997).

[9] L. M. Eng, H.-J. Günterodt, G. A. Schneider, U. Köpke, and J. Muñoz Saldaña, *Appl. Phys. Lett.* **74**, 233 (1999).

[10] Y. Cho, K. Ohara, A. Koike, and H. Odagawa, *Jpn. J. of Appl. Phys.* **40**, 3544 (2001).

[11] K. Ohara and Y. Cho, *Jpn. J. Appl. Phys* **40**, 5833 (2001).

[12] Y. Cho and K. Ohara, *Appl. Phys. Lett.* **79**, 3842 (2001).

[13] H. Odagawa and Y. Cho, *Ferroelectrics*, to be published.

[14] C. S. Ganpule, V. Nagarajan, H. Li, A. S. Ogale, D. E. Steinhauer, S Aggarwal, E. Williams, R. Ramesh, and P. De Wolf, *Appl. Phys. Lett.* **77**, 292 (2000).

[15] Y. Cho, K. Ohara, S. Kazuta, and H. Odagawa, *J. Eur. Ceram. Soc.* **21**, 2135 (2001).

[16] H. Odagawa and Y. Cho, *Jpn. J. Appl. Phys.* **39**, 5719 (2000).

[17] Y. Ishibashi, *J. Phys. Soc. Jpn.* **62**, 1044 (1993).

[18] K. Matsuura, Y. Cho, and H. Odagawa, *Jpn. J. of Appl. Phys.* **40**, 3534 (2001).

[19] H. Odagawa and Y. Cho, *Appl. Phys. Lett.* **80**, 2159 (2002).

[20] Y. Furukawa, K. Kitamura, E. Suzuki, and K. Niwa, *J. Cryst. Growth* **197**, 889 (1999).

[21] K. Kitamura, Y. Furukawa, K. Niwa, V. Gopalan, and T. E. Mitchell, *Appl. Phys. Lett.* **73**, 3073 (1998).

[22] V. Gopalan, T. E. Mitchell, and K. E. Sicakfus, *Solid State Commun.* **109**, 111 (1999).

[23] S. Kim, V. Gopalan, K. Kitamura and Y. Furukawa, *J. Appl. Phys.* **90**, 2949 (2001).